Supplementary Information

Long-Range Wavelike Propagation of Carriers in Methylammonium Lead Iodide Perovskites Thin Films

Jooyoung Sung[1,2], Christoph Schnedermann[1,2], Limeng Ni[1], Aditya Sadhanala[1,3], Richard Y.S. Chen[1], Changsoon Cho[1,4,†], Lee Priest[2], Jong Min Lim[2,‡], Hyun-Kyung Kim[5,‖], Bartomeu Monserrat[1], Philipp Kukura[2*], Akshay Rao[1*]

Supplementary Figures

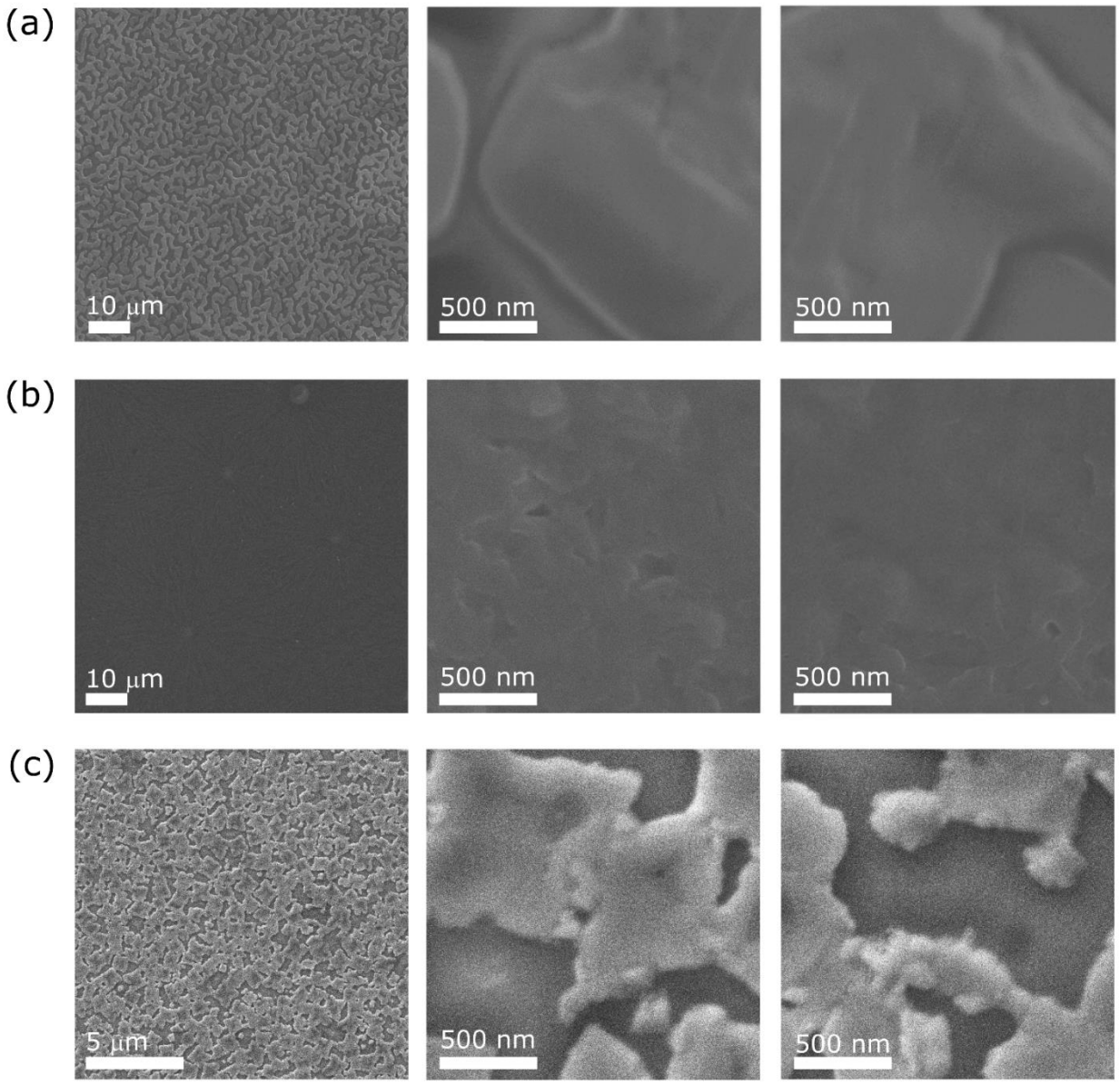

Supplementary Figure 1 : SEM images of films **1** (a), **2** (b) and **3**(c).

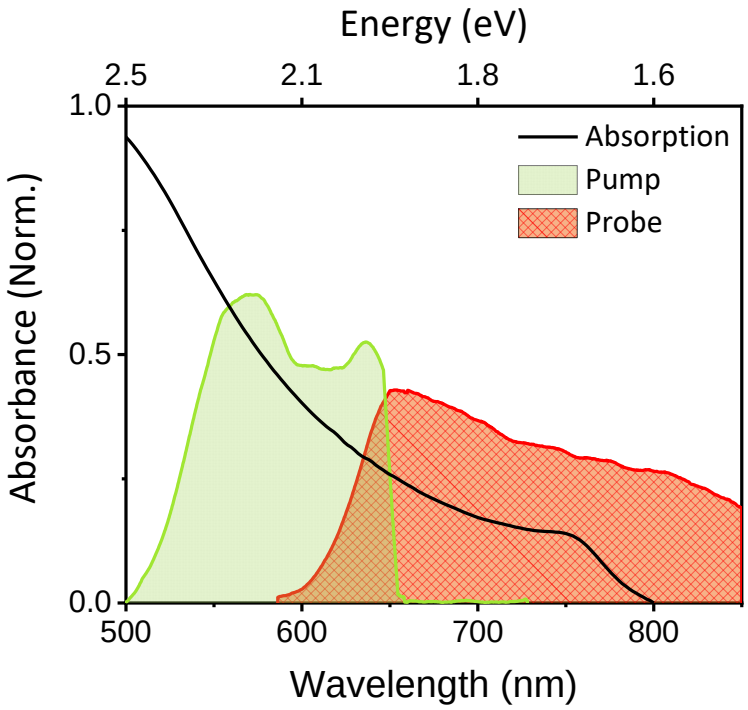

Supplementary Figure 2 : Overlay of the sub-10 fs pump (Green) and probe (Red) pulses with the ground-state absorption spectrum (Black line) of film **1**.

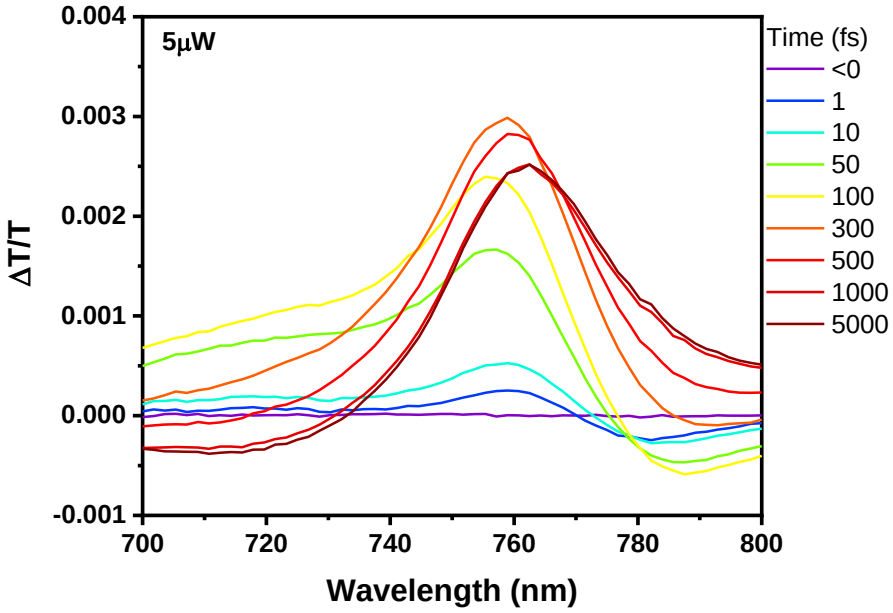

Supplementary Figure 3 : Femtosecond transient absorption spectra of film **1** taken at different pump-probe delays upon photoexcitation at 550 nm (2.25 eV) with a pump fluence of 5 μW.

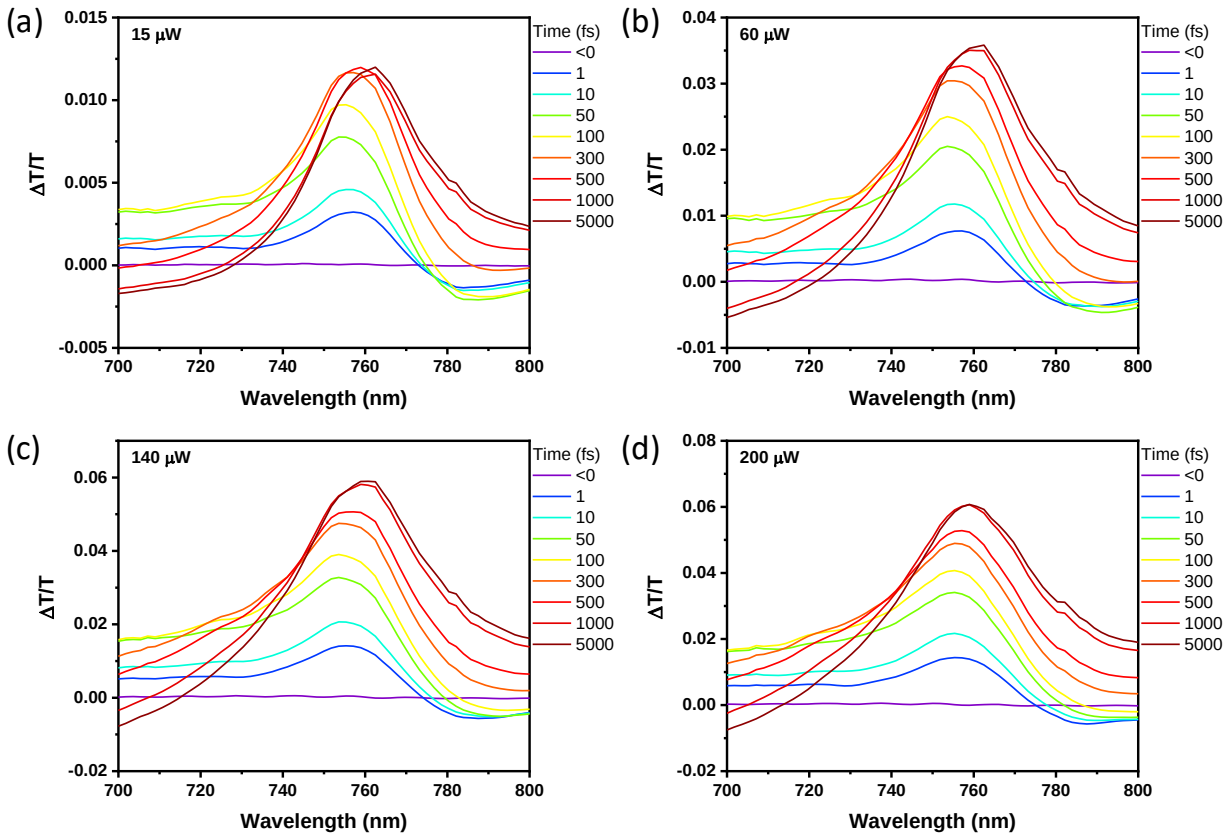

Supplementary Figure 4 : Pump fluence dependent transient absorption spectra of film **1** upon photoexcitation at 550 nm (2.25 eV) with the pump fluences of (a) 15, (b) 60, (c) 140 and (d) 200 μW, respectively.

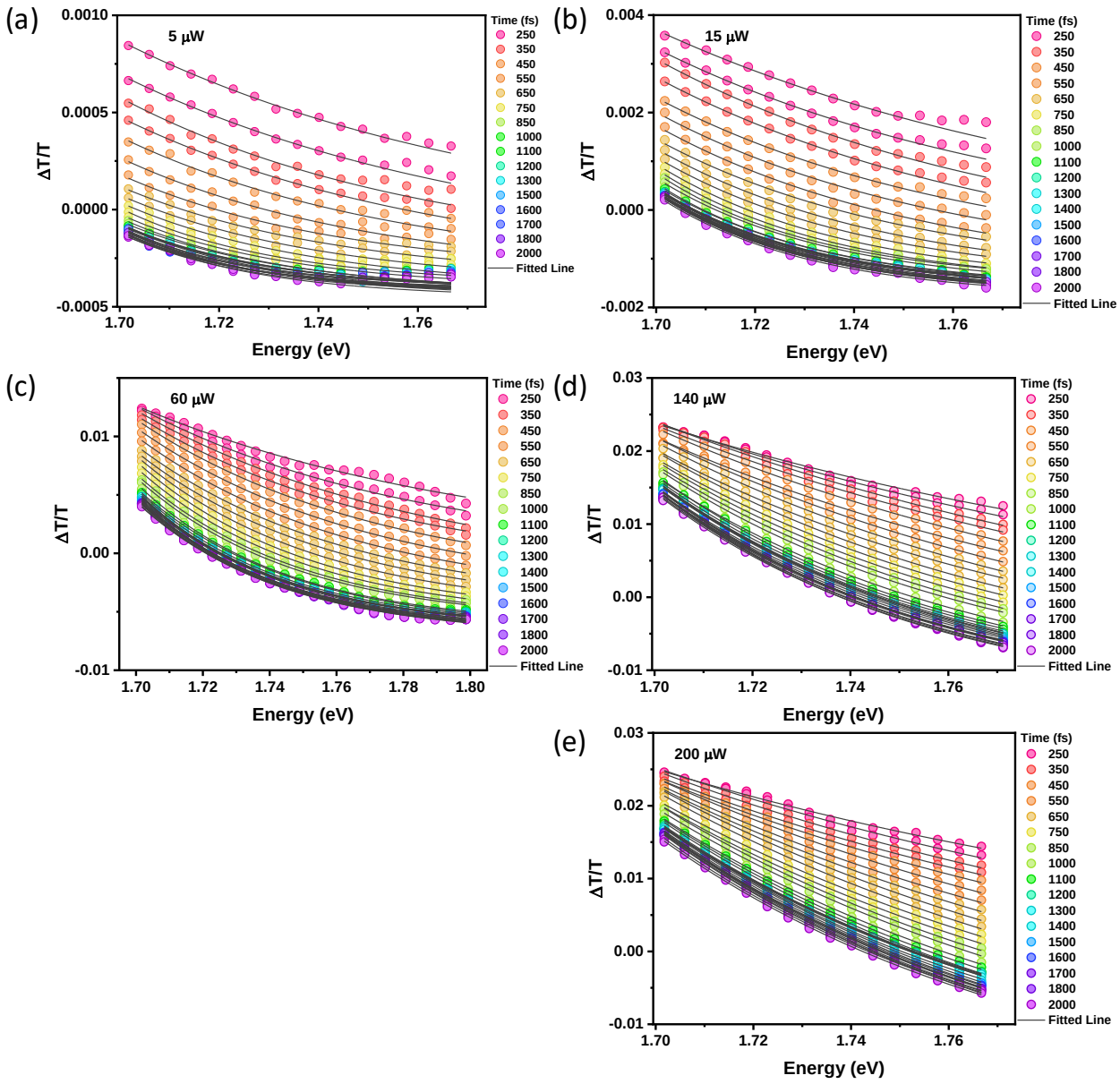

Supplementary Figure 5 : A global fit of the high energy tail of photobleaching band at each timeslice between 260 fs to 2 ps. Pump fluence were varied from (a) 5, (b) 15, (c) 60, (d) 140 and (e) 200 µW, respectively.

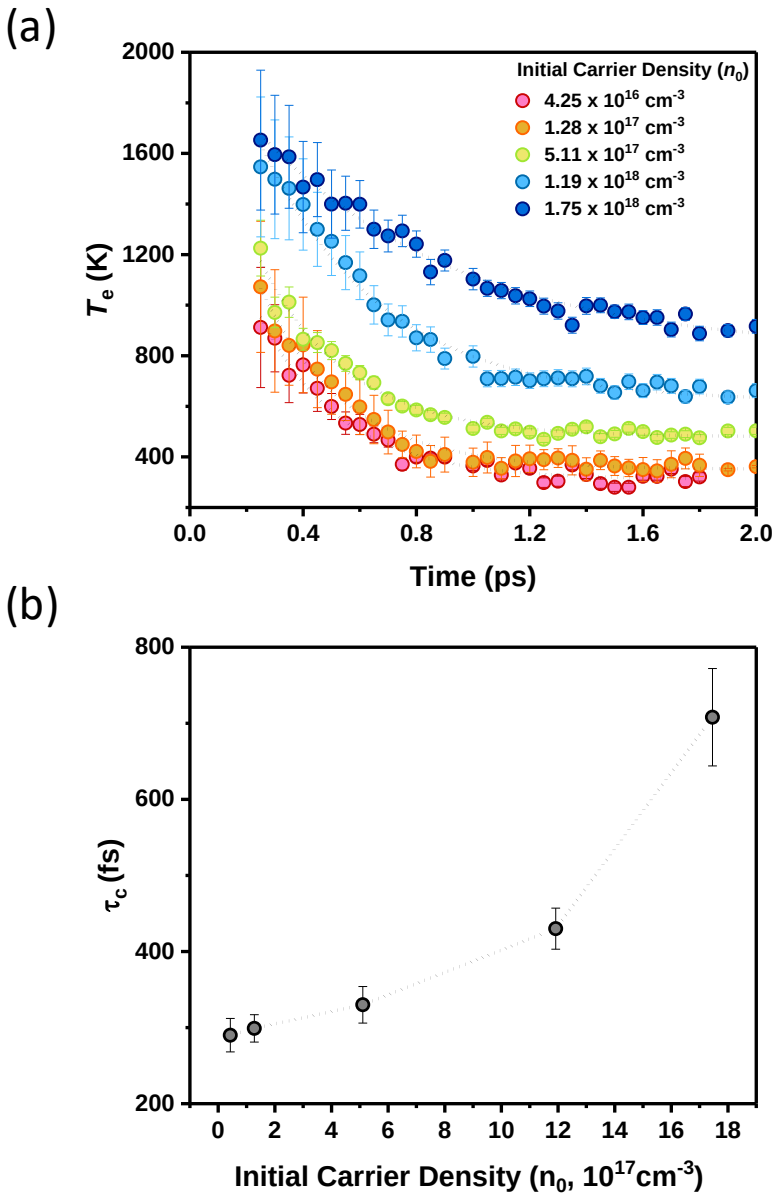

Supplementary Figure 6 : Higher energy tails of photo bleaching peak are fitted by a Maxwell-Boltzmann distribution to extract Te as shown in Supplementary Fig 4. (a) Te decay profiles of carriers with the input carrier densities (n_0) varying between 4.25×10^{16} cm^{-3} to 1.75×10^{18} cm^{-3} (b) Cooling rate for different input carrier obtained from the fit of Te decay profiles.

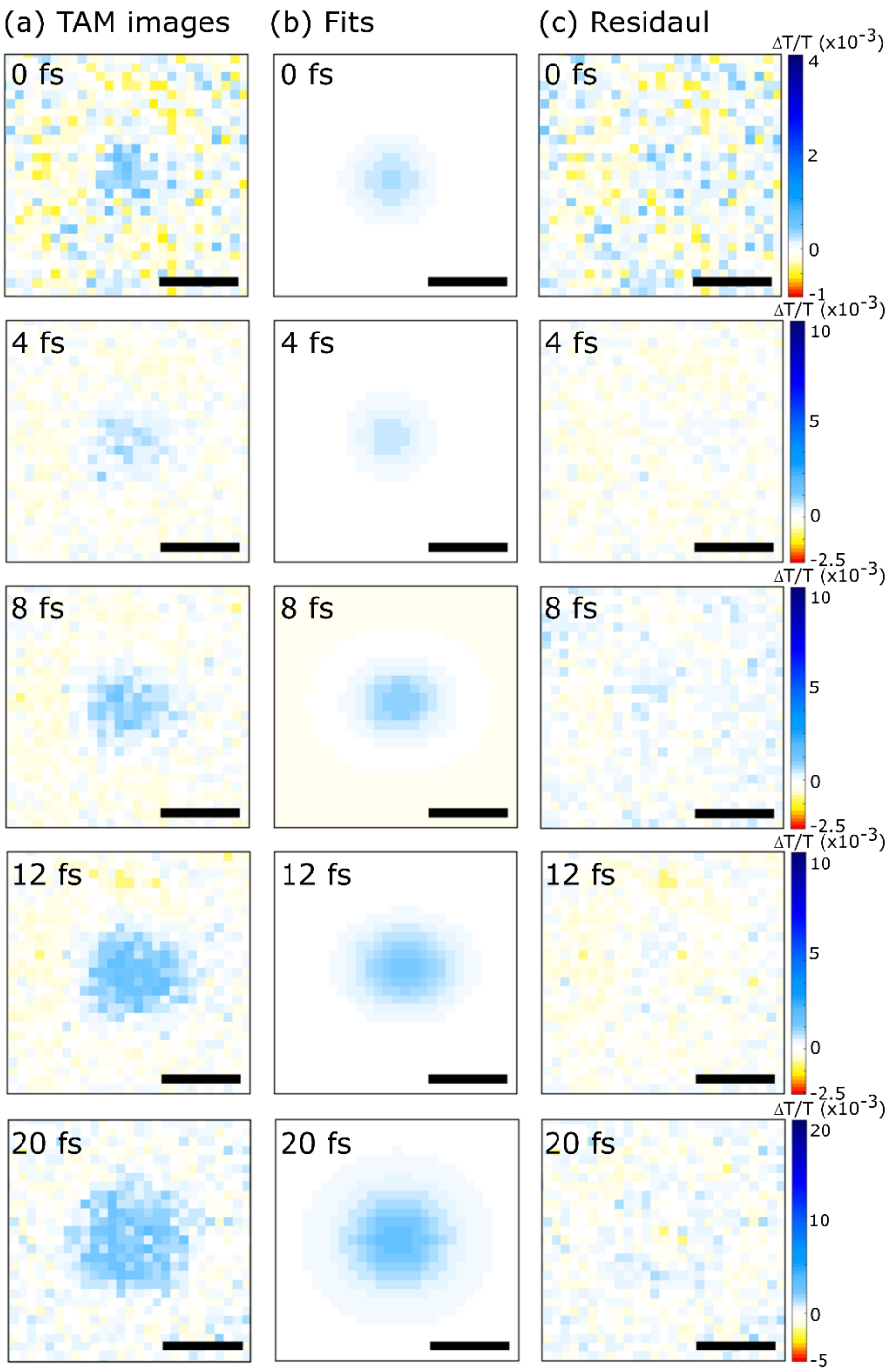

Supplementary Figure 7 : Representative TAM images (a) of film **1** obtained at 720 nm within 20 fs. (b) The corresponding fit images simulated by 2D Gaussian functions. (c) The residual of fits.

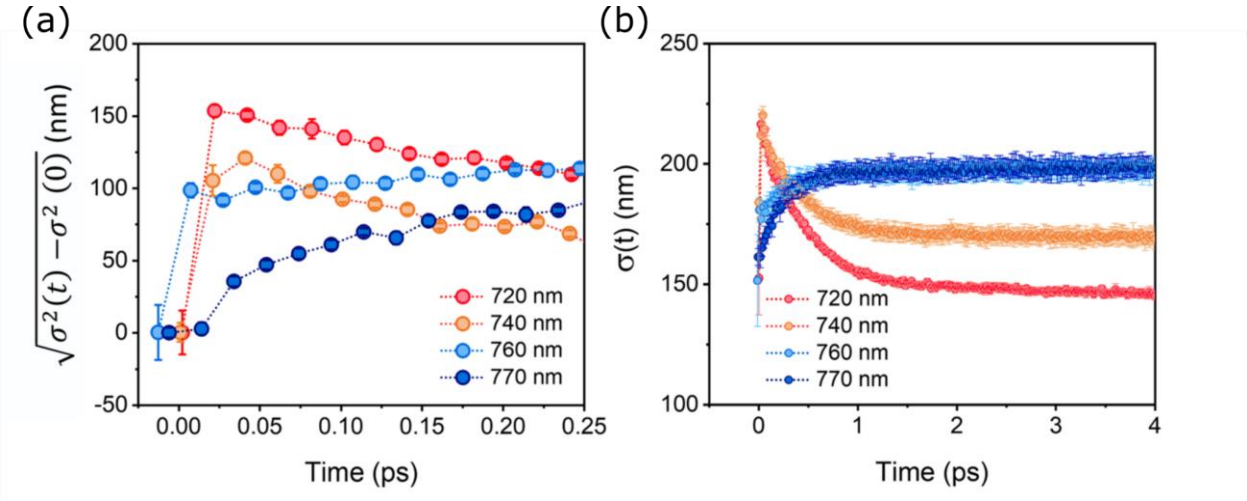

Supplementary Figure 8 : (a) Time evolution of the spatial profile, $\sqrt{(\sigma^2(t)-\sigma^2(0))}$, where $\sigma^2(0)$ is the width of carrier distribution obtained at zero pump-probe delay, during the first 200 fs. (b) Spatial evolution of the carrier distribution, σ(t) during the first 4 ps after photoexcitation. The increase of σ at 770 nm thus corresponds to a cooling of the hot-carriers at 720 nm to 770 nm, rather than motion of carriers at 770 nm.

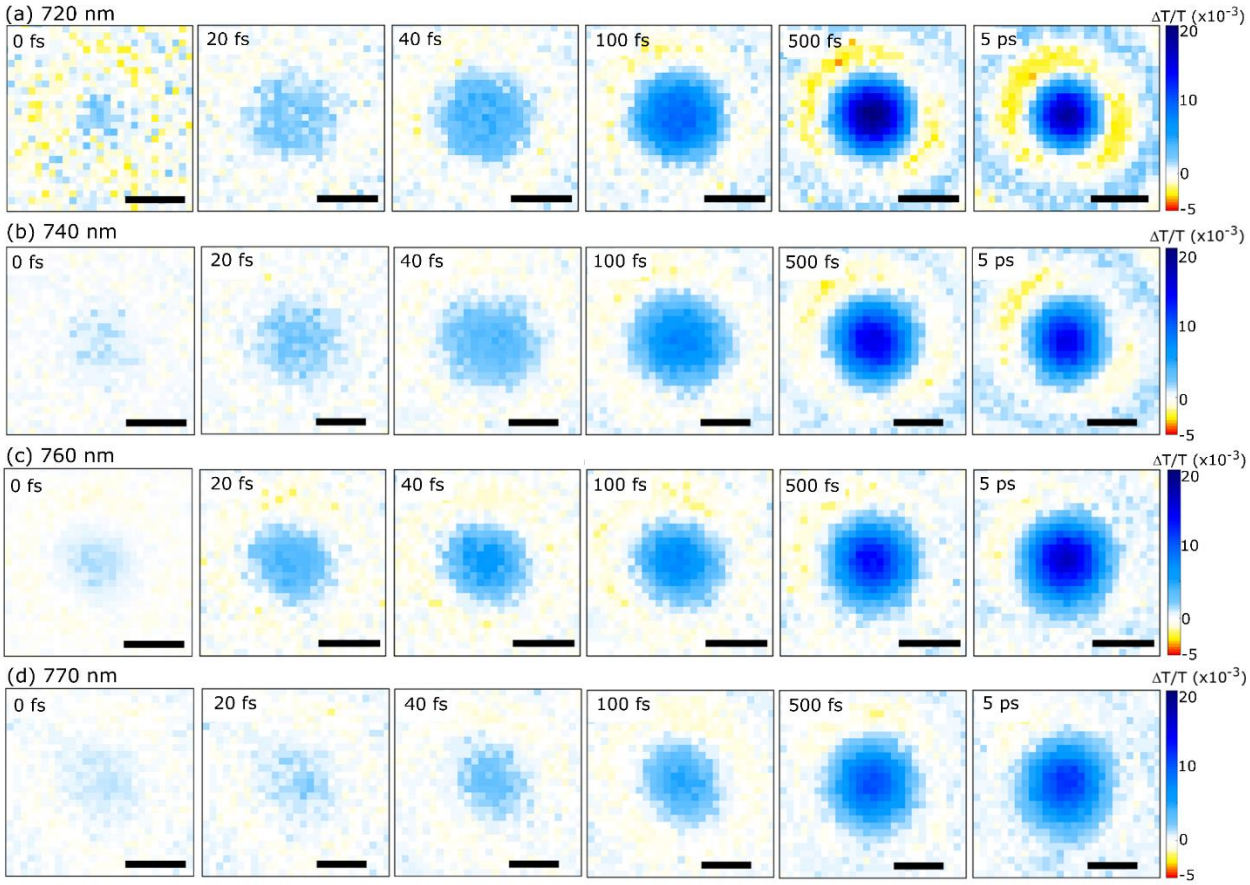

Supplementary Figure 9 : Representative TAM images of film **1** at different time delay, as labeled. Evolution of carrier distribution from high energy side to near band-gap energy (720~770 nm) are presented. Signal intensity of fs-TAM image probing at 720 nm at zero pump-probe delay was scaled by a factor of 5 for clarity. Scale bar, 500 nm

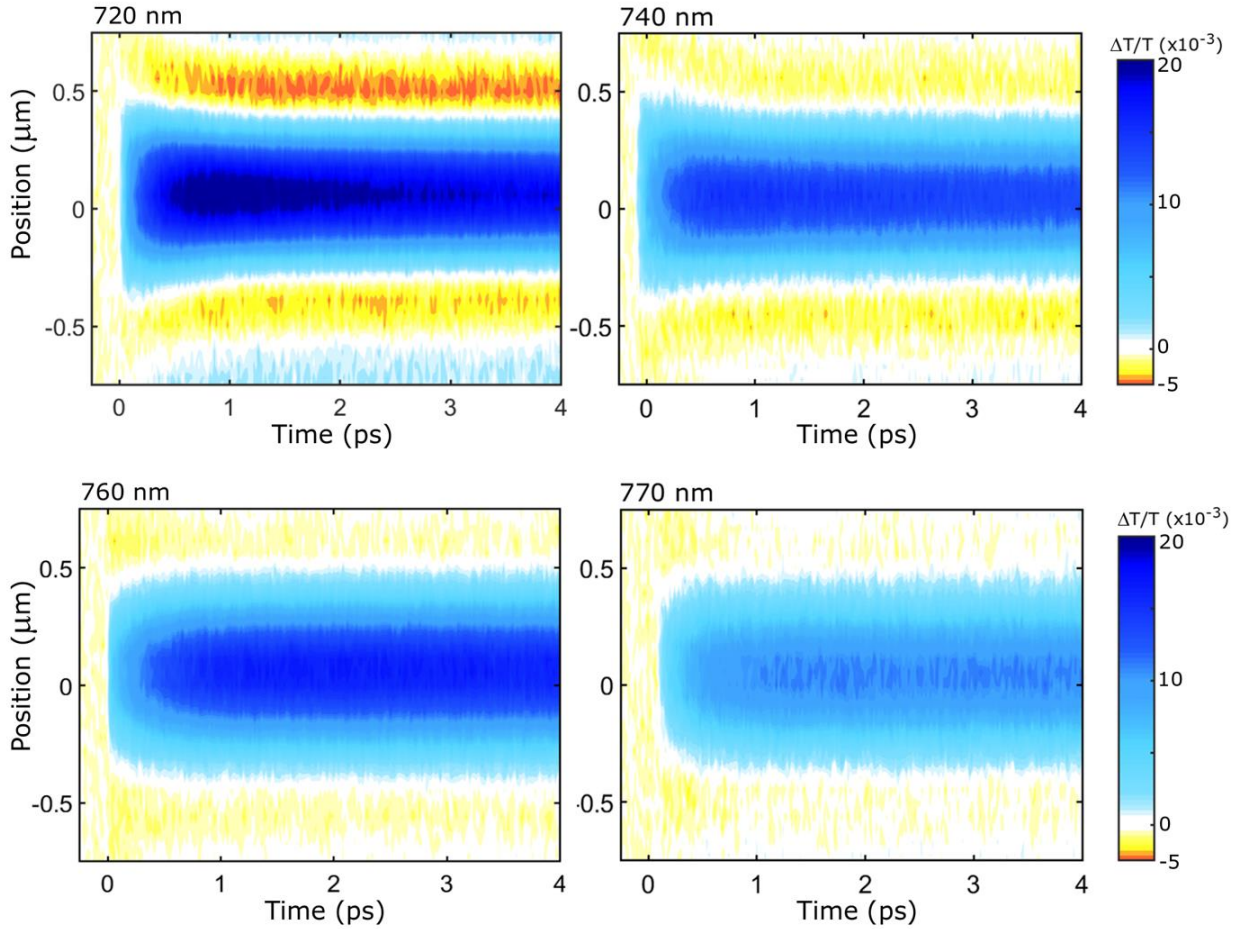

Supplementary Figure 10 : Two-dimensional TAM profiles of film **1** retrieved from one-dimensional cuts at the middle of TAM images.

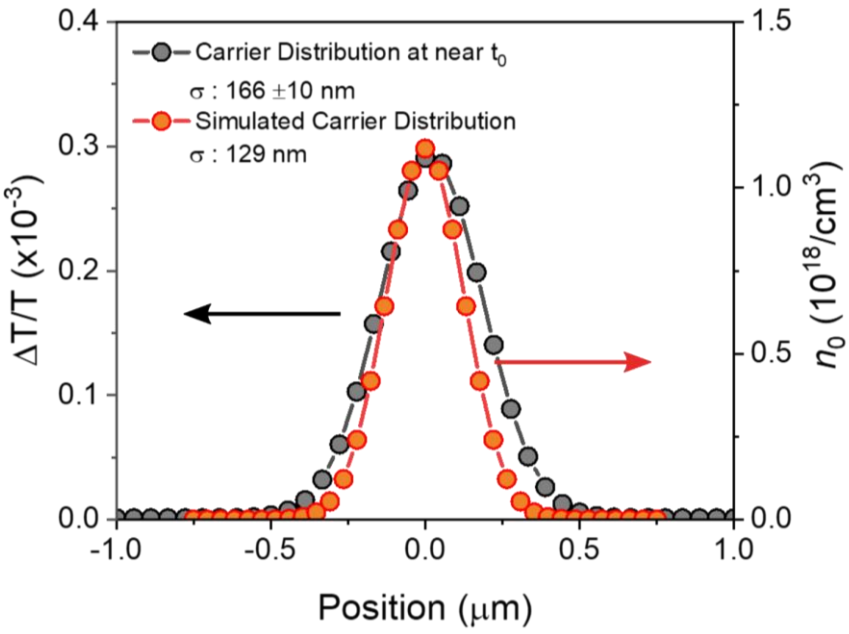

Supplementary Figure 11 : Carrier distribution (black line) obtained by fit of TAM images at time-zero with an isotropic 2D Gaussian function. Theoretical carrier distribution estimated (red line) by convolution between photon distribution of pump beam and extinction coefficients of perovskites (See also Supplementary Fig. 25).

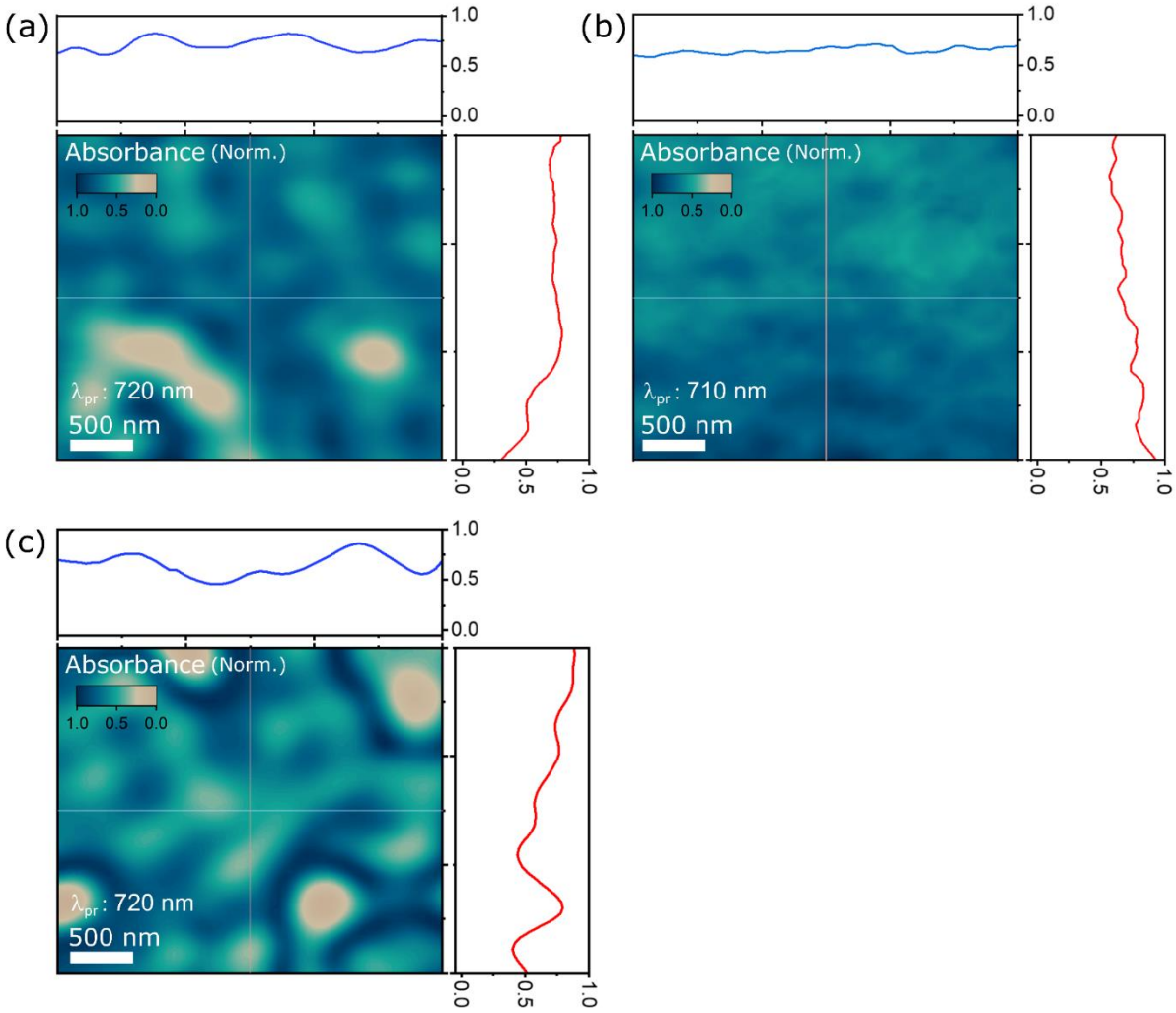

Supplementary Figure 12 : Absorption maps of film **1** (a), **2** (b), and **3** (c) obtained at 720 nm. One dimensional cross cuts of the absorption map are presented in upper and right panel. Whereas absorption distributions are slightly inhomogeneous mainly due to the roughness of films, the absorption distributions within the excitation spot (ca, 129 nm) are relatively homogeneous, providing the quasi-single crystalline condition for the TAM measurement. Scale bar, 500 nm.

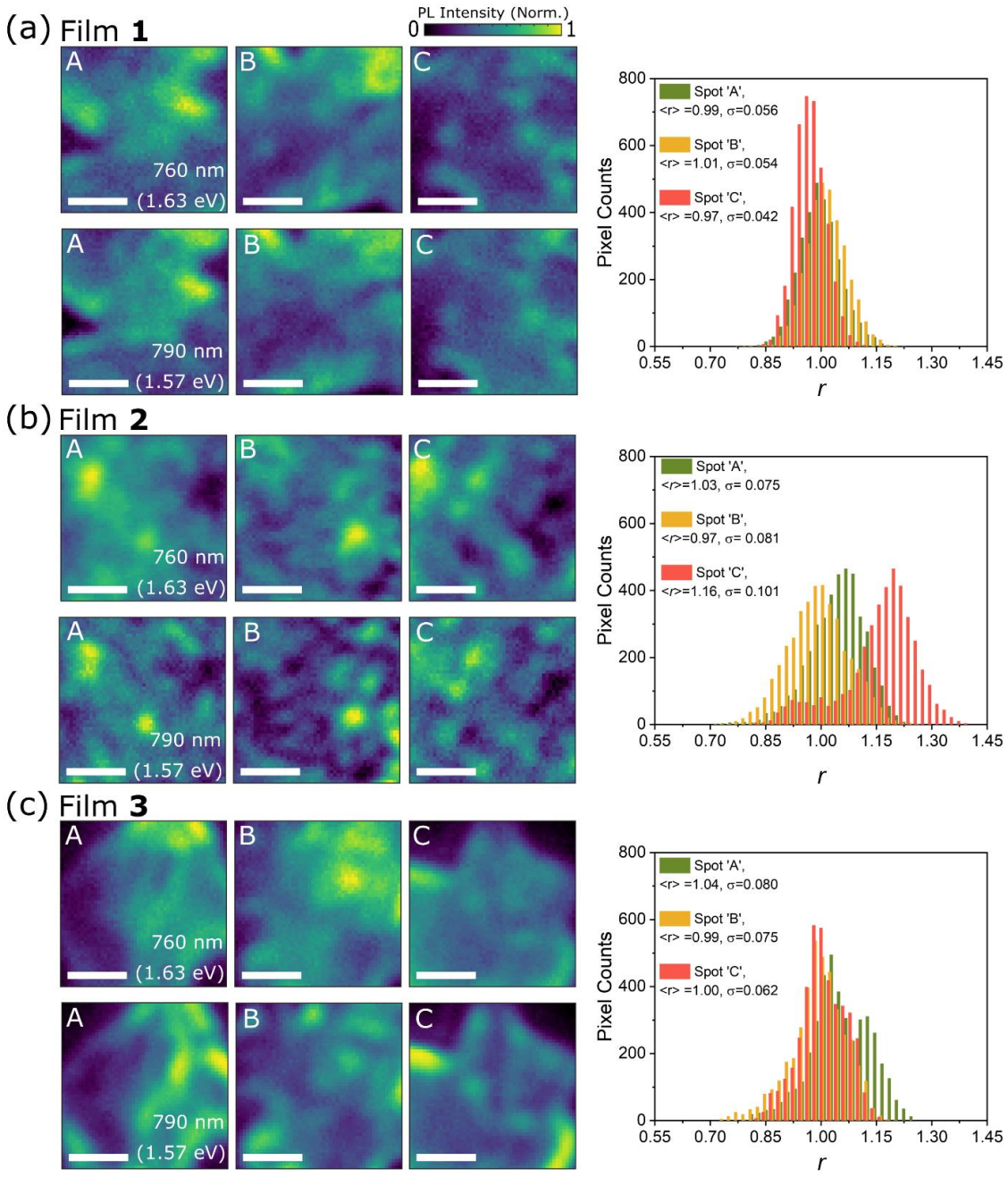

Supplementary Figure 13 : Wide-field fluorescence images of film **1** (a), **2** (b), and **3** (c) at 760 nm (upper panel) and 790 nm (bottom panel). The fluorescence maps are obtained at three different regions (A, B, C) for each films. Scale bar, 500 nm

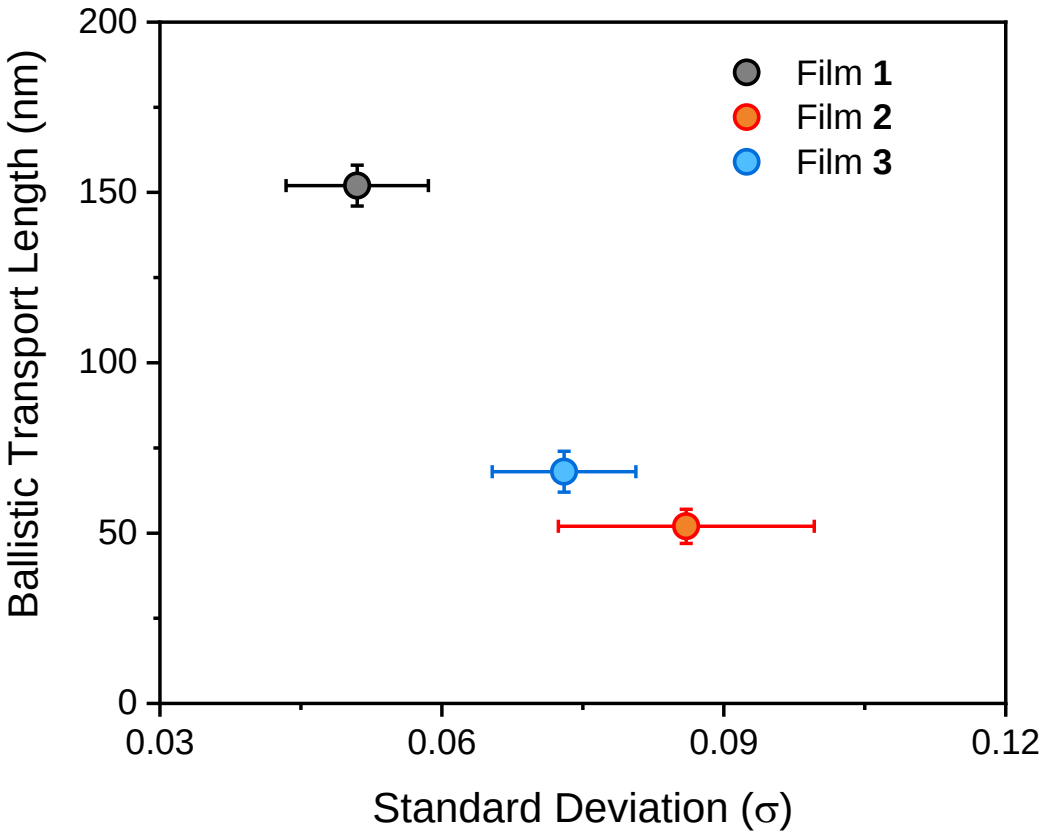

Supplementary Figure 14 : Ballistic transport lengths for film **1**, **2** and **3** plotted as a function of the width of the histogram (See Supplementary Figure 13) . Error bars represent standard deviation widths from obtained from three different regions (A, B, C shown in Supplementary Fig. 13) for each films.

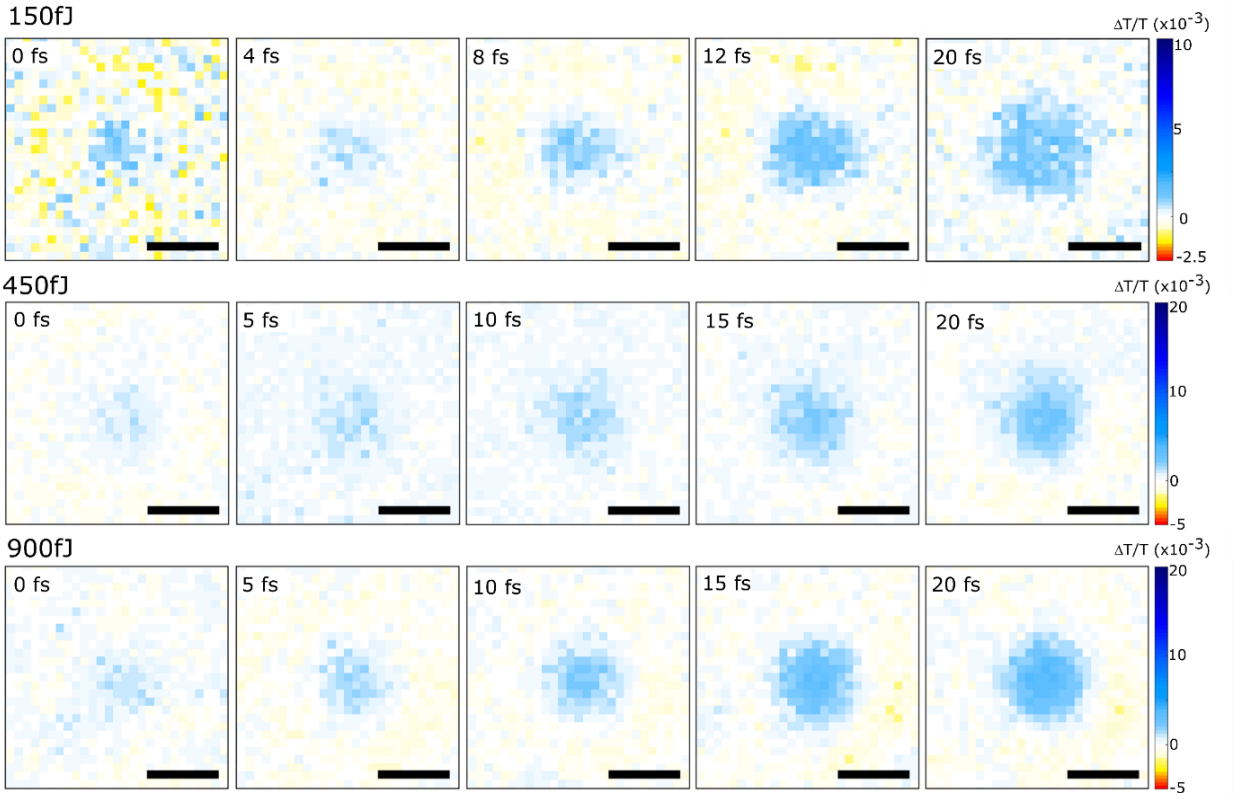

Supplementary Figure 15 : Pump fluence dependent TAM images of film **1** recorded within 20 fs. Representative TAM images at different time delay, as labeled. Evolution of carrier distribution with different carrier density from 5.40×10^{17} (Top), 1.92×10^{18} (Middle), and 2.50×10^{18} cm^{-3} (Bottom). Signal intensity of fs-TAM images at zero pump-probe delay obtained with 150 fJ was scaled by a factor of 2.5 for clarity. Scale bar, 500 nm.

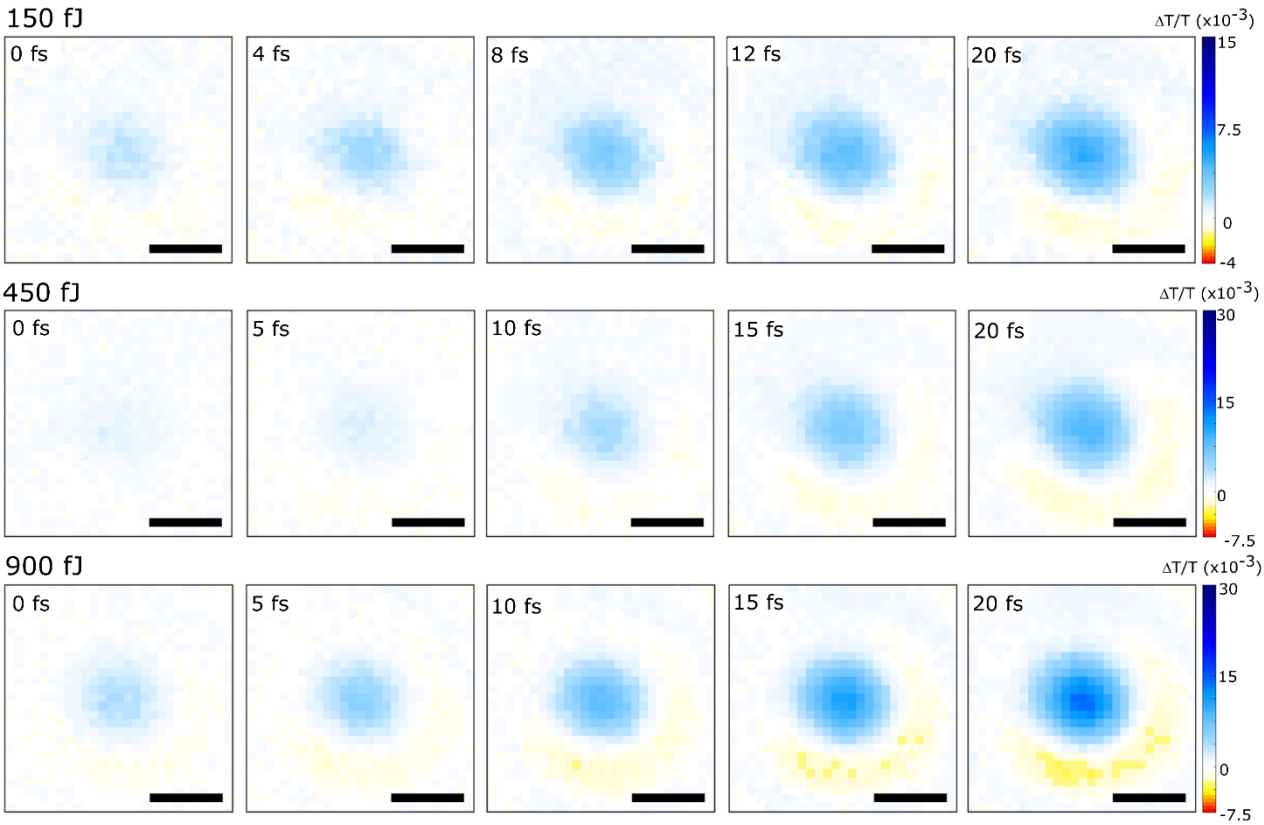

Supplementary Figure 16 : Pump fluence dependent TAM images of film **2** recorded within 20 fs. Representative TAM images at different time delay, as labeled. Evolution of carrier distribution with different carrier density from 5.40×10^{17} (Top), 1.92×10^{18} (Middle), and 2.50×10^{18} cm^{-3} (Bottom). Scale bar, 500 nm.

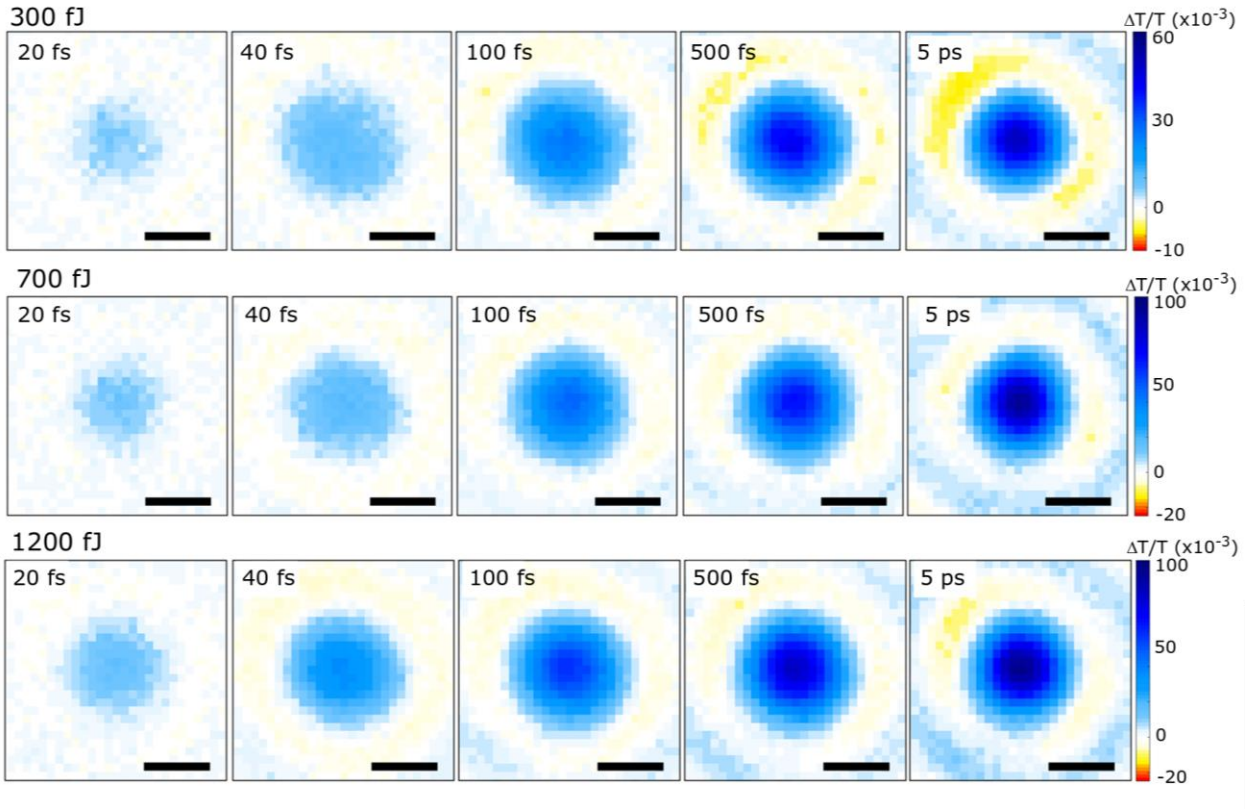

Supplementary Figure 17 : Pump fluence dependent TAM images of film **1**. Representative TAM images at different time delay, as labeled. Evolution of carrier distribution with different carrier density from 1.28×10^{18} (Top), 2.22×10^{18} (Middle), and 2.40×10^{18} cm^{-3} (Bottom). Scale bar, 500 nm.

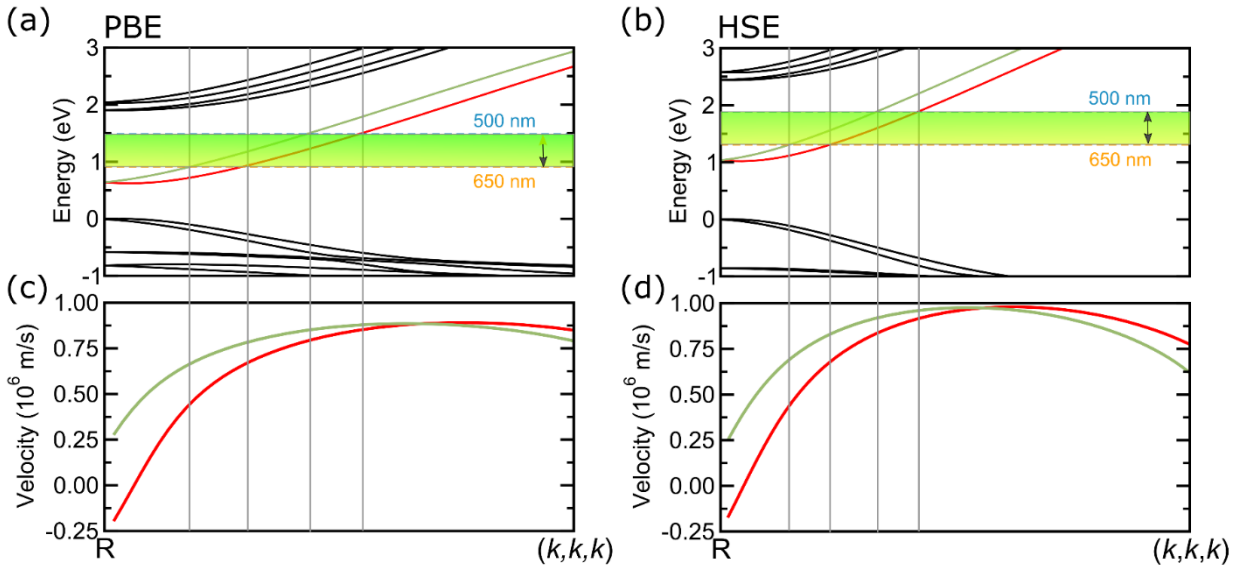

Supplementary Figure 18 : (a) Electronic band structure of cubic MAPI calculated at the semilocal level using PBE approximation. (b) Electronic band structure of cubic MAPI calculated at the hybrid functional level using HSE functional. The two of lowest energy conduction bands are highlighted in red (lowest) and green (second lowest). The two conduction bands are slightly split in energy due to a combination of spin-orbit coupling and inversion symmetry breaking caused by the organic MA+ cation. The horizontal green shade shows the excitation energy at the corresponding energies after renormalizing the calculated conduction band bottom to the experimental value. (c, d) The group velocity of two lowest energy conduction bands derived from the above band structures under the assumption that the primary carriers are electrons.

Supplementary Table 1: Best-fit parameters of σ at around zero pump-probe delay

	720 nm (1.72 eV, 0 fs)	740 nm (1.68 eV, 0 fs)	760 nm (1.63 eV, -2 fs)	770 nm (1.60 eV, - 6 fs)
σ (t)	166.0 ±10.0 nm	184.0 ± 6.5 nm	166.1 ± 12.0 nm	161.3 ± 3.5 nm
σ Diffraction Limit (FWHM)	129 (303) nm	133 (312) nm	136 (320) nm	138 (325) nm

Supplementary Table 2: Best-fit parameters of σ decay profiles

	720 nm (1.72 eV)	740 nm (1.68 eV)	760 nm (1.63 eV)	770 nm (1.60 eV)
τ (fs)	430 ± 10	410 ± 5	220 ± 15 (rise)	230 ± 10 (rise)

Supplementary Information:

1. Determination of the pump size. Pump beam size was determined based on the fluorescence intensity profile obtained by scanning the pump across a bead (TetraSpeck^{TM} fluorescent microspheres, T7179, ~ 100 nm). Since the fwhm of the cross-correlation function between the bead and the pump pulse is measured to be 270 nm (σ: 115 nm) (Supplementary Fig.1), the effective pump size at sample is about 250 nm (σ_p: 107 nm).

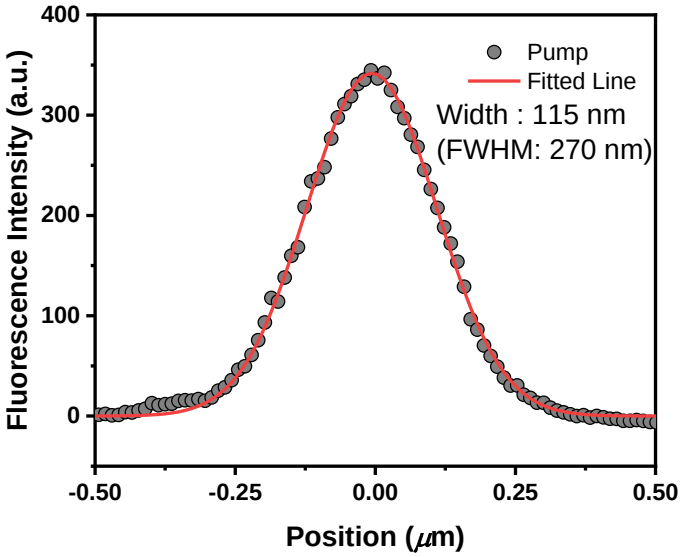

Supplementary Figure 19 : Fluorescence intensity profile of a fluorescent bead (TectraSpeck^{TM} Microspheres, T7179). By scanning pump beam across the bead, the convoluted fluorescence intensity profile is obtained.

2. Pulse characterization

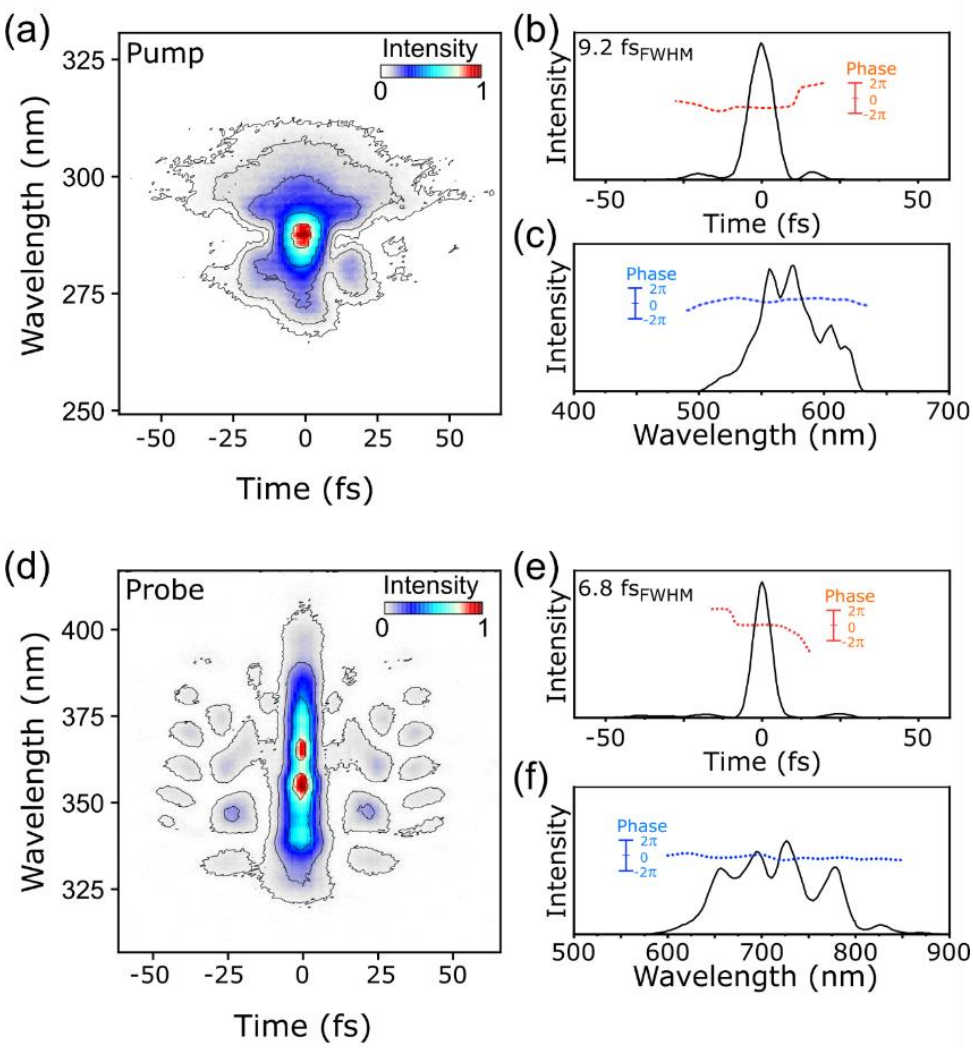

Supplementary Figure 20 : (a) SHG-FROG trace of pump obtained after compression. (b) Temporal profile (black solid line) and phase (red dotted line) retrieved from the SHG-FROG trace of pump. (c) The SHG-FROG spectrum (black solid) and phase (blue dotted line), retrieved from the SHG-FROG trace of pump. (d) SHG-FROG trace of probe obtained after compression. (e) Temporal profile (black solid line) and phase (red dotted line) retrieved from the SHG-FROG trace of probe. (f) The SHG-FROG retrieved spectrum (black solid) and phase (blue dotted line), retrieved from SHG-FROG trace of pump.

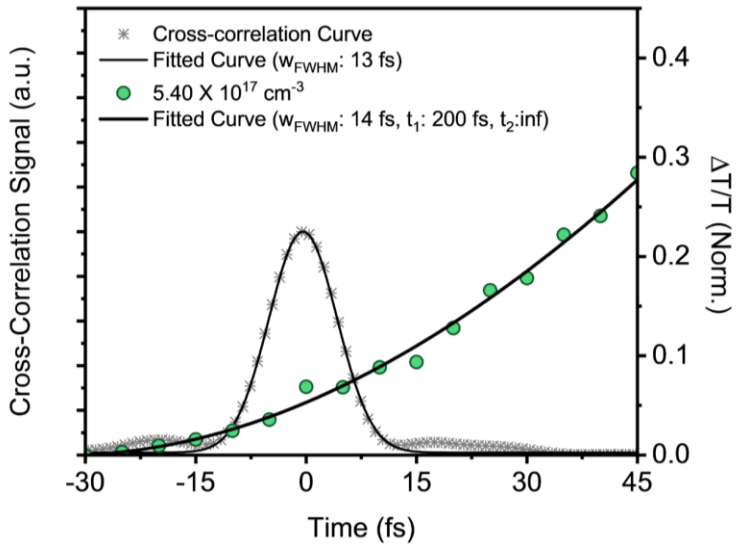

Supplementary Figure 21 :**.** The simulated cross-correlation curve with the retrieved pump and probe temporal profiles (star dot line) and the early-time transient absorption kinetics at 720 nm obtained from TAM measurement (green dot line). The fit of cross-correlation curve reveals the fwhm of 13 fs. Consistent with this temporal resolution, the deconvolution fit for the transient absorption kinetics at 720 nm shows the fwhm of 14 fs.

3. Fitting of the TAM profiles to extract σ_t. The carrier distribution *n(x,y,t)* can be approximated by a two dimensional Gaussian function, $N\exp\left[-\frac{(x-x_0)^2}{2\sigma_{x,t}^2}-\frac{(y-y_0)^2}{2\sigma_{y,t}^2}\right]$. The measured intensity distribution function results from the convolution among the profiles of pump, probe and carries, that is $\sigma_{I,t}^2=\sigma_{pump,t}^2+\sigma_{probe,t}^2+\sigma_{carrier,t}^2$. However, since pump and probe do not changes over time, the evolution of $\sigma_{I,t}^2-\sigma_{I,0}^2$ exclusively represents the change in the carrier density distribution.

4. Determination of the spatial precision. As briefly described above, the measured image is the spatial convolution of the carrier, pump and probe photon distribution functions. Since the variance of convoluted Gaussians is additive, one can find that the variance of the measured distribution

functions is the sum of the carrier, pump and probe distribution functions; $\sigma_{I,t}^2 = \sigma_{pump,t}^2 + \sigma_{probe,t}^2 + \sigma_{carrier,t}^2$. Under the assumption that the pump and probe distribution does not evolved over time, we can find that the evolution in carrier distribution can be directly obtained from the measured intensity variance;

$$\Delta\boldsymbol{\sigma}_{\boldsymbol{carrier,t}}^{\boldsymbol{2}} = \boldsymbol{\sigma}_{\boldsymbol{carrier,t}}^{\boldsymbol{2}} - \boldsymbol{\sigma}_{\boldsymbol{carrier,0}}^{\boldsymbol{2}} = \boldsymbol{\sigma}_{\boldsymbol{I,t}}^{\boldsymbol{2}} - \boldsymbol{\sigma}_{\boldsymbol{I,0}}^{\boldsymbol{2}}$$

We note here that the evolution in carrier distribution does not depend on the initial pump and probe distribution. Spatial precision for time-resolved imaging techniques has been previously discussed by G. M. Akselrod et al.[1], where a photoluminescence microscopy imaging technique was employed and Z. Guo. et al.[2], where transient absorption microscopy was employed. An error analysis for the combined uncertainty of measurement for the evolution in carrier distribution ($\Delta(\Delta\sigma_{carrier,t})$) can be calculated in the follow steps [3],

$$\Delta\boldsymbol{\sigma}_{\boldsymbol{carrier,t}} = \sqrt{\boldsymbol{\sigma}_{\boldsymbol{I,t}}^{\boldsymbol{2}} - \boldsymbol{\sigma}_{\boldsymbol{I,0}}^{\boldsymbol{2}}} = \boldsymbol{f}(\boldsymbol{\sigma}_{\boldsymbol{I,t}}, \boldsymbol{\sigma}_{\boldsymbol{I,0}})$$

$$\Delta\left(\Delta\boldsymbol{\sigma}_{\boldsymbol{carrier,t}}\right) = \sqrt{\sum_{\boldsymbol{i}}\left(\frac{\boldsymbol{\partial f}}{\boldsymbol{\partial\sigma_{I,i}}}\Delta\boldsymbol{\sigma}_{\boldsymbol{I,i}}\right)} = \sqrt{\frac{\boldsymbol{\sigma}_{\boldsymbol{I,t}}}{\sqrt{\boldsymbol{\sigma}_{\boldsymbol{I,t}}^{\boldsymbol{2}} - \boldsymbol{\sigma}_{\boldsymbol{I,0}}^{\boldsymbol{2}}}}\left(\Delta\boldsymbol{\sigma}_{\boldsymbol{I,t}}\right) + \frac{\boldsymbol{\sigma}_{\boldsymbol{I,0}}}{\sqrt{\boldsymbol{\sigma}_{\boldsymbol{I,t}}^{\boldsymbol{2}} - \boldsymbol{\sigma}_{\boldsymbol{I,0}}^{\boldsymbol{2}}}}\left(\Delta\boldsymbol{\sigma}_{\boldsymbol{I,t}}\right)}$$

$$= \sqrt{\frac{\boldsymbol{\sigma}_{\boldsymbol{I,t}}\Delta\boldsymbol{\sigma}_{\boldsymbol{I,t}} + \boldsymbol{\sigma}_{\boldsymbol{I,0}}\Delta\boldsymbol{\sigma}_{\boldsymbol{I,0}}}{\sqrt{\boldsymbol{\sigma}_{\boldsymbol{I,t}}^{\boldsymbol{2}} - \boldsymbol{\sigma}_{\boldsymbol{I,0}}^{\boldsymbol{2}}}}} = \sqrt{\frac{\boldsymbol{\sigma}_{\boldsymbol{I,t}}\Delta\boldsymbol{\sigma}_{\boldsymbol{I,t}} + \boldsymbol{\sigma}_{\boldsymbol{I,0}}\Delta\boldsymbol{\sigma}_{\boldsymbol{I,0}}}{\Delta\boldsymbol{\sigma}_{\boldsymbol{carrier,t}}}}$$

According to the above expression for the combined uncertainty of measurement, we determine the spatial precision of our measurement for the evolution in carrier distribution as shown in Supplementary Fig. 22.

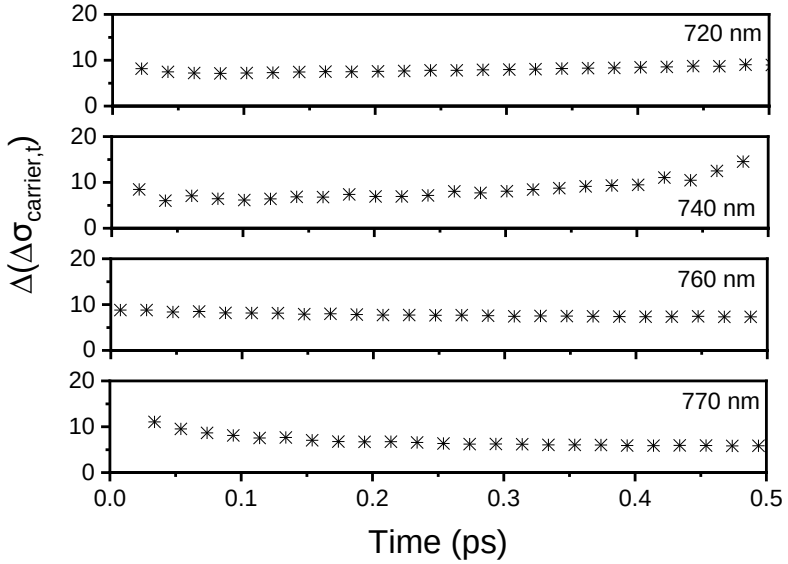

Supplementary Figure 22 : The traces of the combined measurement precision of the measurement system obtained at 720, 740, 760 and 770 nm, respectively.

In addition, we also present the width profiles of the carrier distribution and the residual components extracted from exponential fits in order to show the spatial precision of individual measurements (Supplementary Fig. 23). Both these methods show that we can achieved a spatial localization precession of 10 nm.

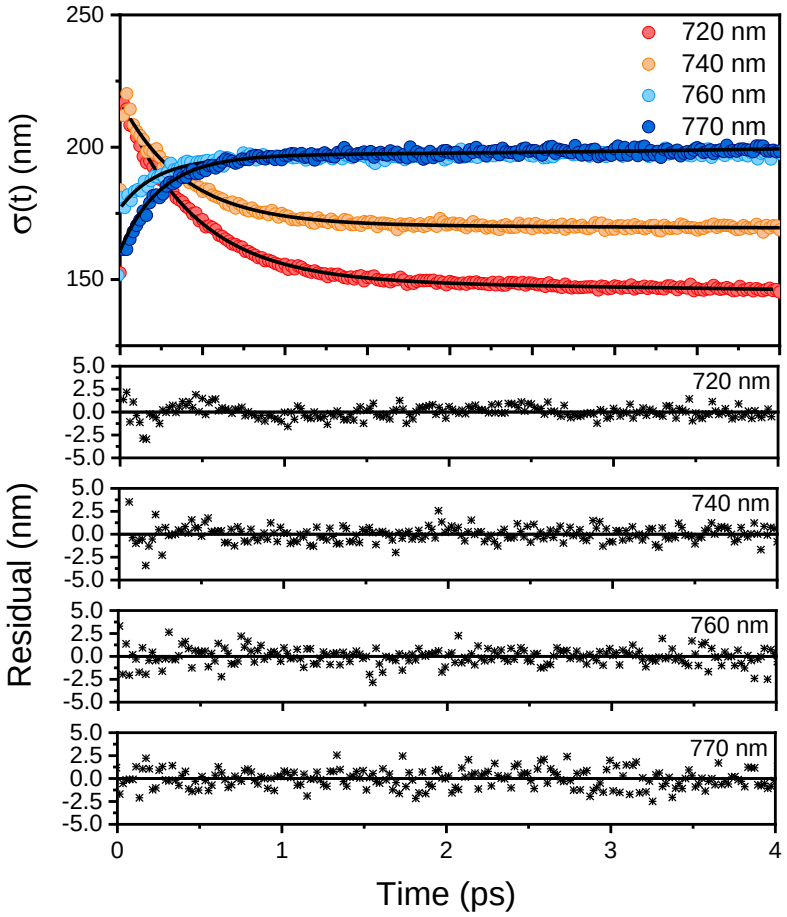

Supplementary Figure 23 : (Top) The width profiles of carrier distribution, σ(t), and the fitted lines. (Bottom) The fit residuals for the measurements at 720, 740, 760 and 770 nm.

5. Characterization of transient species. The primary photogenerated species in 3D hybrid halide perovskites are free electrons and holes due to the low exciton binding energy (i.e., several meV), which is smaller than k_BT, although the exact values for the exciton binding energies are still matter of debate. We begin by reviewing salient features of the transient absorption spectra of perovskite thin films obtained by transient absorption (TA) measurement using 15 fs pulses. Upon photoexcitation of the perovskite thin film at 550 nm (ca. 2.25 eV) with an initial carrier density (n_0) of 1.28×10^{17} cm^{-3}, two general spectral features are observed at early times before 500 fs; a sharp photobleach (PB) peak between 750-770 nm with the high-energy tail over the range from

650 nm, and a negative TA feature below E_g. The broad high-energy tail of the PB band is mainly attributed to band-filling effects originating from a quasi-equilibrium carrier distribution. After several hundreds of femtoseconds, this positive feature for high-energy tail of PB band becomes negative. This feature is largely attributed to hot carrier cooling in the continuum. Furthermore, unlike organic semiconducting materials, the transient reflectivity changes of inorganic semiconducting materials with large refractive index are significant. As the transient reflectivity changes for the perovskite thin film become dominant, it eventually overwhelms the transient absorptivity changes and renders transient transmission feature negative, consistent with the previous observation. Furthermore, the exchange and correlation energies stemming from the hot carrier generation minimize the total energy of perovskite thin films and hence narrow the band-gap. This band-gap renormalization creates new transition between the modified band edge states resulting in a negative photo-induced absorption feature below E_g. When the initial quasi-equilibrium carrier distribution evolves, the gradual occupation of renormalised band edge states takes places. Thus, the negative feature below E_g becomes positive within 500 fs in agreement with the previous reports.

6. Pump fluence dependent behavior of carrier dynamics. In order to quantitatively correlate free carrier dynamics with carrier density, we have performed fluence-dependent transient absorption measurements within the initial carrier densities ranging from 4.25×10^{16} cm^{-3} to 1.75×10^{18} cm^{-3} (Supplementary Figs. 3, and 4). Since the high-energy side of PB band is directly correlated with electron and hole Fermi distribution and can be approximated by a Maxwell-Boltzmann distribution function, the elevated carrier temperature (T_e) was extracted by fitting the spectral shape of high-energy side PB after 250 fs with a Maxwell-Boltzmann distribution

(Supplementary Fig. 4**)**. As shown in Supplementary Fig. 5 and 6, it is evident that the carrier cooling process has a strong dependence on the carrier density. The hot carriers at relatively low carrier density of 4.25×10^{16} cm^{-3} relax to the lattice temperature (i.e., 300 K) with the decay constant of 290 fs. Upon increasing the initial carrier density to 1.75×10^{18} cm^{-3}, the cooling processes become slower. At high carrier densities over 1.75×10^{18} cm^{-3}, the carriers require several picoseconds to cool down. This apparent decrease in the cooling rate can be explained by a phonon bottleneck effect. At high carrier density, the high phonon emission rate is accompanied by non-equilibrium population of phonons. This excess hot-phonon population induces phonon reabsorption and therefore suppresses the net phonon emission process. We note here that other well-known carrier density dependent behaviors such as bi-molecular and Auger charge recombination processes have a non-significant effect on the charge carrier dynamics within the temporal region of our interest. For instance, a clear experimental signature of the involvement of Auger charge recombination process is an increasing weight of the fast component upon increasing pump fluence.[15-17] However, as shown in Supplementary Fig. 24, there is no increasing weight of

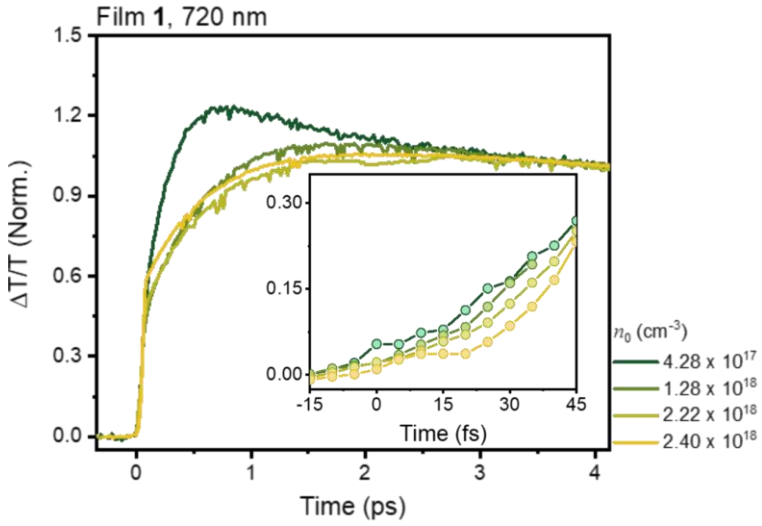

Supplementary Figure 24 : Normalized transient absorption kinetics at 720 nm plotted as a function of carrier density obtained from fs-TAM measurement.

a fast decay component apparent in the transient absorption kinetics at 720 nm. Instead, the transient kinetics within 50 fs exhibit similar feature except the slower growth at high carrier density which is due to slower cooling.

7. Density functional theory. First principles simulations were performed for the cubic and tetragonal structures of $MAPbI_3$ to calculate the band structure and the corresponding band velocities (Supplementary Fig. 18). We used density functional theory[4,5] and the projector augmented-wave method[6,7] as implemented in the VASP package[8,9]. Our results were obtained with an energy cut-off of 400 eV and an electronic Brillouin zone sampling grid of size 6x6x4. The exchange correlation functional was described at the semilocal level using the Perdew-Burke-Ernzerhof (PBE) approximation[10] and at the hybrid functional level using the Heyd-Scuseria-Ernzerhof (HSE) functional[11]. We included spin-orbit coupling using the second variational method in all calculations[12].

PBE calculations for the cubic and tetragonal structures give similar results. The HSE functional leads to more accurate band structures, but at a larger computational cost. For this reason, we have performed the computationally expensive HSE calculations using the higher-symmetry cubic phase of $MAPbI_3$ only, and assumed that changing to the tetragonal phase will not result in significant differences in line with the PBE results. For the cubic phase, the band gap minimum is located around the R (1/2,1/2,1/2) point (which gets folded into the Gamma point in the tetragonal structure). We have performed calculations along lines joining the R point to the (0,0,0), (0,0,1/2), (0,1/2,0), (1/2,0,0), (1/2,1/2,0), (1/2,0,1/2), and (0,1/2,1/2) points in the Brillouin zone. Supplementary Fig. 18 (a) and (b) show the PBE and HSE results for the line joining R to (0,0,0) as a representative case. The HSE band velocity (Supplementary Fig. 18c and d) is between

$0.60*10^6$ and $1.00*10^6$ ms^{-1} depending on the excitation energy, and approaches $1.00*10^6$ ms^{-1} at somewhat higher energies. The corresponding band velocities at the PBE level of theory are slightly smaller.

8. Wavelength dependent behavior of non-equilibrium carriers. In order to quantify the spatiotemporal evolution of each carrier distribution at different probe energies, we fitted the resulting TAM images using a 2D Gaussian function and extracted their standard deviation, σ (Supplementary Fig. 7). The standard deviation of the TA image at zero pump-probe delay, σ(0), representative of the underlying carrier distribution for each probe wavelength, exhibited similar values close to the diffraction limit (Supplementary Table 1). As observed in transient absorption spectroscopy measurements (Fig. 1b), carrier generation leads to an initial PB peak. Accordingly, in the fs-TAM data, the peak around zero-time delay was spatially distributed only within the pump area, which represents the initial carrier distribution. The relative changes in the standard deviationof the carrier distribution (Fig. 2 and Supplementary Fig. 8), revealed the carrier transport distance. Surprisingly, 20 fs after the photoexcitation, the width of the carrier distribution at 720 nm increased by 150 ± 4 nm. At energies closer to E_g, the corresponding width changes were smaller, 105 and 72 ± 10 nm at 740 and 760 nm, respectively.

The thermalization process originating from carrier-carrier scattering allows us to track the initial ballistic transport of non-equilibrium carriers by monitoring the dynamics of the high-energy tail of the PB band (ca. 1.72 to 1.68 eV). As carriers move out of the area occupied by the original carrier distribution, carrier-carrier scattering leads to carrier thermalization on a timescale of tens of fs. The associated band-filling phenomena accompanying carrier thermalization result in the

appearance of the PB signal in areas outside the original carrier distribution and hence where at zero time no signal is present. Since the carriers thermalize to a distribution peaked close to but above E_g and occupy fewer states near the band edge (Fig. 1c), the initial expansion in the TAM images is most pronounced at 720 nm and becomes less pronounced the closer we probe near E_g.

As shown in Supplementary Figs. 8-10, following the initial expansion within 20 fs, we observed the opposite spatiotemporal behaviour for the high energy tail of the PB peak and E_g (760 nm). At 720 nm, the standard deviation, σ, decreased to the diffraction limit (ca. 129 nm) with a time constant of 435 ± 10 fs, but at E_g increased up to 200 nm with a 230 ± 15 fs time constant (Supplementary Table 2). This behaviour can be understood considering that following thermalisation the temperature of carriers remains higher than the lattice temperature, commonly referred to as hot-carriers (Fig. 1c)[20]. Subsequent cooling of the hot-carriers is achieved predominantly through carrier-LO phonon scattering on the 200 - 400 fs timescale, in good agreement with the σ(t) dynamics (Supplementary Figs. 8)[24,26,28]. The increase of σ at E_g thus corresponds to a cooling of the hot-carriers at 720 nm to energies at E_g. Importantly, the maximum σ of the carrier distribution at E_g does not exceed the maximum σ of the carrier distribution at 720 nm within 5 ps. We thus conclude that there is no significant transport of hot-carriers within the first 5 ps after the initial ultrafast ballistic transport of non-equilibrium carriers.

9. Spatially varying cooling rates. Within the experiments presented here, the initial photon distribution of the pump pulse follows a Gaussian distribution and the fs-TAM images reveal a Gaussian carrier distribution even after initial ballistic transport. Thus, it is clear that the number of carriers per unit volume (i.e., carrier density distribution) varies as we move away from the

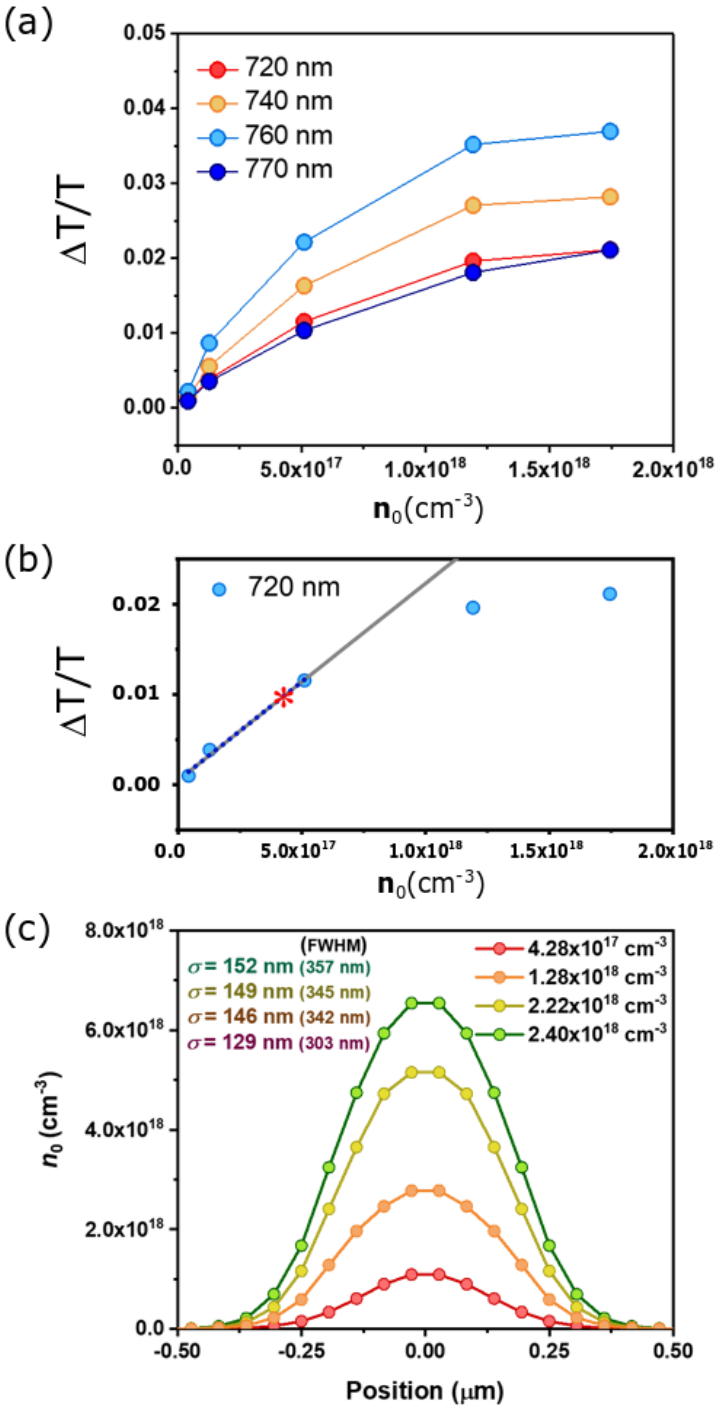

Supplementary Figure 25 : (a) Transient absorption intensity (ΔT/T) obtained at 100 fs plotted as a function of carrier density at four different probing wavelength. (b) Transient absorption intensity (ΔT/T) obtained at 100 fs plotted as a function of carrier density at 720 nm. The grey line shows the linear fit curve of the trace. Asterisk (*) indicates the lowest fluence used for the fs-TAM measurement. (c) Simulated carrier density distribution map for different input carrier density.

center of the pump pulse. As there is a spatially varying carrier distribution, this will lead to a

spatially varying rate of carrier cooling. We therefore simulated the carrier density map so as to draw a correlation between carrier density and cooling rate. As shown in Supplementary Fig. 25a, pump fluence dependent transient absorption measurement allow us to extract the relationship between $\Delta T/T$ and carrier density. By comparing $\Delta T/T$ at each pixel of the TAM image with the above curve, we were able to convert $\Delta T/T$ into the corresponding carrier density and therefore simulate the carrier density distribution map (Supplementary Fig. 25c).

The simulated carrier density map shows the maximum density of 1.1×10^{18} cm^{-3} at the pump center while the carriers at a probing position of 1.4 w_0 (w_0 is the waist of Gaussian distribution at $1/e^2$) exhibit five times lower carrier density (i.e., 2.68×10^{17} cm^{-3}). In order to systematically analyze the effect of carrier density on the dynamics, we have compared the decay profiles of the PB band integrated over all angles at four different sections as described in Supplementary Fig. 25a. The double exponential behaviors of decay profiles represent carrier cooling process although this exponential model does not fully include spatial carrier transport effect (Supplementary Figs. 26b, 26c and 26d). Supplementary Fig. 27 clearly reveals that the cooling rate becomes faster when probing away from pump center, consistent with the observation of fluence dependent transient absorption measurement on the perovskite thin film.

Returning to the fs-TAM data presented in Supplementary Figure 8, 9 and 10, we note the opposite behaviors of FWHM traces between high energy tail of PB band (720 nm) and E_g (760 nm). This behavior can now be understood to arise due to the spatially varying carrier cooling rate. As the carriers toward the outside of the 760 nm distribution cool faster than the carriers at the center of the distribution, this leads to a shape change for the distribution and an apparent contraction of the carrier distribution on the ps timescale. Concomitantly, the faster cooling of the higher energy

carriers to lower energy carriers leads to a faster rise of the 760 nm signal at the edge of the distribution and hence the apparent growth in the 760 nm distribution on the ps timescale.

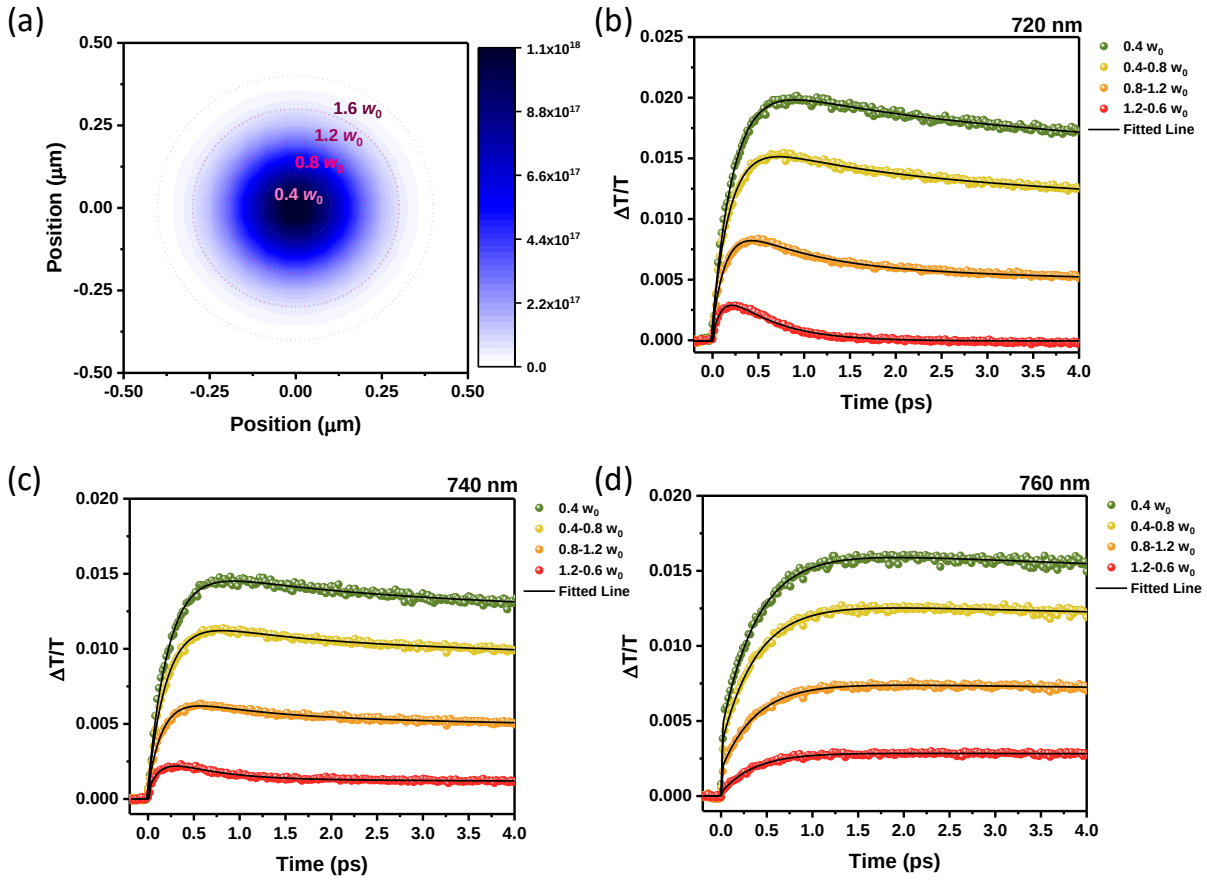

Supplementary Figure 26 : (a) Schematic density distribution representing 4 different density regime. Kinetics of MAPI obtained at each regimes for (b) 720, (c) 740 and (d) 760 nm. The decay profiles were obtained by integrating over all angles at four different regime. The double exponential behaviors of decay profiles well represent carrier cooling process although this exponential model does not fully include spatial carrier transport effect.

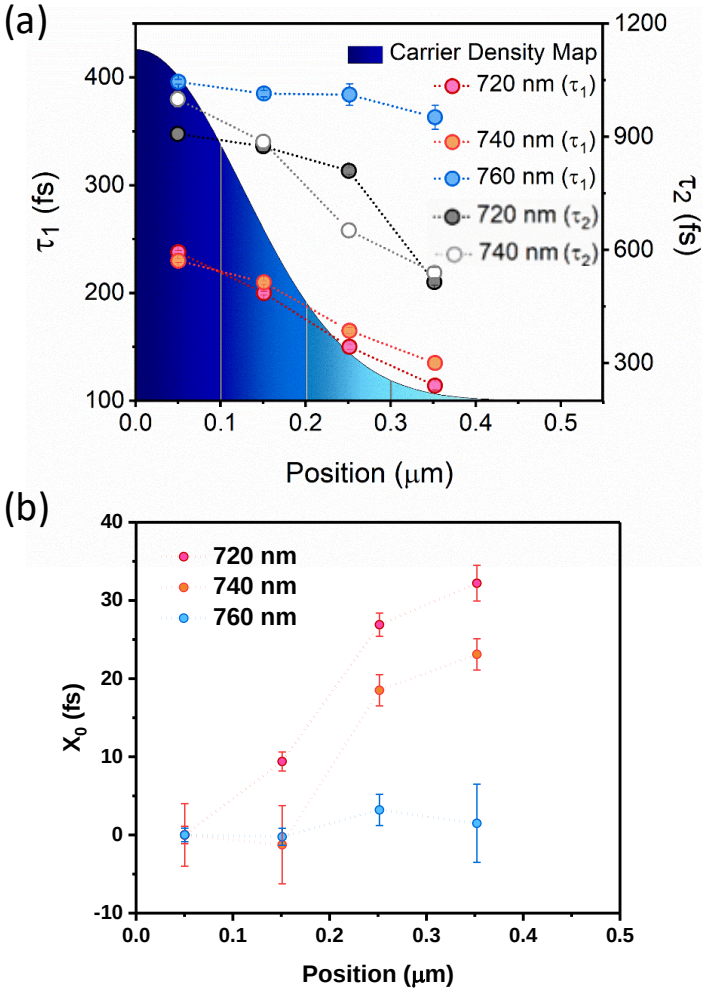

Supplementary Figure 27 : (a) Different time constants obtained at different position of carrier distribution. (b) Relative time zero components obtained from the double-exponential fit as shown in Supplementary Fig. 26. The relative time zero components at 760 nm are constant over space, which indicates that carrier population at 760 nm rise simultaneously. On the other hands, the relative time zero components at 720 and 740 nm are varied over different position; the carrier population at center rise first around time-zero while the carrier population at 1.6 w_0 region start to appear 30 fs later than the one at the center. This observation implies the ultrafast carrier transport motion within several tens of femtosecond.

10. Efficiency of charge collection due to ballistic motion of charge carriers following photoexcitation. A simple charge collection model has been developed for the ballistic transport of carriers to the charge collection electrodes. If a carrier is formed at a distance x from a front

contact layer, the probabilities of it reaching the front interface (P_{front}(x)) and back interface (P_{back}(x)), can be expressed as follows,

$$P_{front}(x) = \Omega_{front} / 4\pi,$$

$$P_{back}(x) = \Omega_{back} / 4\pi,$$

where Ω_{front} and Ωback are the solid angles of the cone defined by the ballistic trajectories of charge carriers capable of reaching the front and back interfaces, which become $2\pi(1 - x / B.T.D.)$ and $2\pi(1 - (h - x) / B.T.D.)$, respectively, for isotropic motion, where h is the thickness of perovskite and B.T.D is the ballistic transport distance. Therefore,

$$P_{front}(x) = \begin{cases} \frac{1}{2}\left(1 - \frac{x}{B.T.D.}\right), & x < B.T.D. \\ 0, & x \geq B.T.D. \end{cases}$$

$$P_{back}(x) = \begin{cases} \frac{1}{2}\left(1 - \frac{h - x}{B.T.D.}\right), & x > h - B.T.D. \\ 0, & x \leq h - B.T.D. \end{cases}$$

Thus, the overall efficiency, ε, is given by,

$$\varepsilon_{front} = \frac{\int_0^h P_{front}(x)G(x)dx}{\int_0^h G(x)dx}$$

$$\varepsilon_{back} = \frac{\int_0^h P_{back}(x)G(x)dx}{\int_0^h G(x)dx}$$

where G(x) indicates the generation profile of charge carriers under given illumination. We calculated G(x) using transfer-matrix formalism (TMF)[13] for an arbitrary photovoltaic device

structure of glass / indium tin oxide (ITO, 150 nm) / poly(3,4-ethylenedioxythiophene):poly(styrenesulfonate) (PEDOT:PSS, 40 nm) / perovskite / [6,6]-phenyl-C71-butyric acid methyl ester ($PC_{70}BM$, 100nm) / Ag, under 1 sun illumination with AM1.5G spectrum. The refractive index of perovskite was obtained from literature[14].

Supplementary Fig. 28a shows the calculated G(x) for h = 400 nm. While the interference between the incident and reflected lights is shown, G(x) is shown to be the highest at x = 0 and decay rapidly. Hence, the collection efficiency is calculated to be much higher for the front interface (ε_{front} = 22.1%) than for the back interface (ε_{back} = 3.0%), when B.T.D. = 150 nm. Supplementary Fig. 28b shows the variation of the collection efficiencies as a function of h in the same device structure, for the fixed B.T.D. of 150 nm. While both ε_{front} and ε_{back} are shown to be high (ε_{front} + ε_{back} ~ 100%) for h << B.T.D., it drops rapidly as h increases. It should be noted that at least 20% of ε_{front} is maintained for the B.T.D. of 150 nm regardless of h, while ε_{back} becomes zero for large h, since charge carriers are mostly generated near the front interface and the incident light hardly reaches the deeper region.

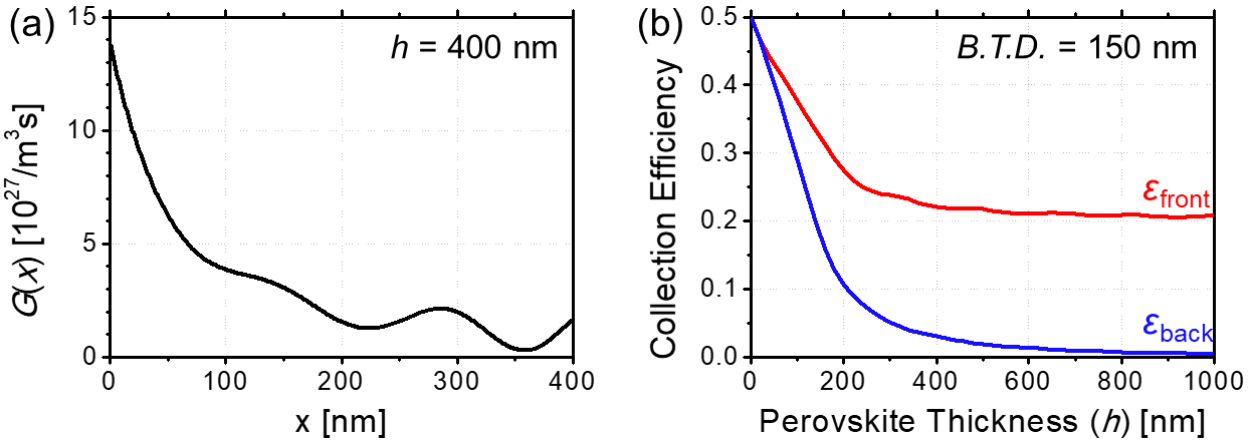

Supplementary Figure 28 : (a) Charge generation profile (*G*) in the 400 nm perovskite layer of the photovoltaic device structure under AM1.5G illumination. (b) Charge collection efficiencies at the front and back interfaces as a function of the thickness of perovskite layer with the B.T.D. of 150 nm.

References

1. Akselrod, G. M. *et al.* Visualization of exciton transport in ordered and disordered molecular solids. *Nat. Commun.* **5,** 3646 (2014).
2. Guo, Z., Manser, J. S., Wan, Y., Kamat, P. V. & Huang, L. Spatial and temporal imaging of long-range charge transport in perovskite thin films by ultrafast microscopy. *Nat. Commun.* **6,** 1–8 (2015).
3. Jcgm, J. C. F. G. I. M. Evaluation of measurement data — Guide to the expression of uncertainty in measurement. *Int. Organ. Stand. Geneva ISBN* **50,** 134 (2008).
4. A. K. Rajagopal, J. Callaway, Inhomogeneous electron gas. *Phys. Rev. B.* **7**, 1912–1919 (1973).
5. W. Kohn, L. J. Sham, Self-consistent equations including exchange and correlation effects. *Phys. Rev.* **140** (1965), doi:10.1103/PhysRev.140.A1133.
6. P. E. Blöchl, Projector augmented-wave method. *Phys. Rev. B.* **50**, 17953–17979 (1994).
7. D. Joubert, From ultrasoft pseudopotentials to the projector augmented-wave method. *Phys. Rev. B - Condens. Matter Mater. Phys.* **59**, 1758–1775 (1999).
8. G. Kresse, J. Hafner, Ab initio molecular-dynamics simulation of the liquid-metal–amorphous-semiconductor transition in germanium. *Phys. Rev. B.* **49**, 14251–14269 (1994).
9. G. Kresse, J. Hafner, Ab initio molecular dynamics for liquid metals. *Phys. Rev. B.* **47**, 558–561 (1993).
10. J. P. Perdew, K. Burke, M. Ernzerhof, Generalized gradient approximation made simple. *Phys. Rev. Lett.* **77**, 3865–3868 (1996).
11. J. Paier, M. Marsman, K. Hummer, G. Kresse, I. C. Gerber, J. G. Angyán, Screened hybrid density functionals applied to solids. *J. Chem. Phys.* **124**, 154709-154709 (2006).
12. A. H. Macdonald, W. E. Picket, B. C. H. Krutzen, F. Springelkamp, T. Takeda, Technique for relativistic spin-polarised calculations. *J. Phys. C Solid State Phys.* (1977).
13. L. A. A. Pettersson, L. S. Roman, O. Inganas,Modeling photocurrent action spectra of photovoltaic devices based on organic thin films. *J. Appl. Phys.* **86**, 487-496 (1999).
14. C. W. Chen, S. Y. Hsiao, C. Y. Chen, H. W. Kang, Z. Y. Huang, H. W. Lin, Optical properties of organometal halide perovskite thin films and general device structure design rules for perovskite single and tandem solar cells. *J. Mater. Chem. A.* **3**, 9152-9159 (2015).
15. E. Serpetzoglou, I. Konidakis, G. Kakavelakis, T. Maksudov, E. Kymakis, E. Stratakis, sImproved carrier transport in perovskite solar cells probed by femtosecond transient absorption spectroscopy. *ACS Appl. Mater. Interfaces* **9**, 43910−43919 (2017)
16. V. A. Hintermayr, L. Polavarapu, A. S. Urban, J. Feldmann, Accelerated carrier relaxation through reduced coulomb screening in two dimensional halide perovskite nanoplatelets, *ACS Nano* **12**, 10151−10158 (2018)
17. C. Wehrenfennig, G. E. Eperon, M. B. Johnston, H. J. Snaith, L. M. Herz, High Charge carrier mobilities and lifetimes in organolead trihalide perovskites *Adv. Mater*. **26**, 1584–1589 (2014)